









RESEARCH ARTICLE | DECEMBER 23 2024

Approximate calculation of backpropagated energy spectrum for a proton beam

E. Nichelatti ; M. Piccinini ; A. Ampollini ; M. D. Astorino ; G. Bazzano ; P. Nenzi ; V. Surrenti; E. Trinca ; C. Ronsivalle 



J. Appl. Phys. 136, 244901 (2024)
<https://doi.org/10.1063/5.0241408>



Articles You May Be Interested In

Design and test of a compact beam current monitor based on a passive RF cavity for a proton therapy linear accelerator

Rev. Sci. Instrum. (November 2021)

Photoluminescent Bragg curves in lithium fluoride thin films on silicon substrates irradiated with a 35 MeV proton beam

J. Appl. Phys. (July 2022)

A 3D printed pure copper drift tube linac prototype

Rev. Sci. Instrum. (February 2022)



Journal of Applied Physics

Special Topics Open for Submissions

[Learn More](#)

Approximate calculation of backpropagated energy spectrum for a proton beam

Cite as: J. Appl. Phys. 136, 244901 (2024); doi: 10.1063/5.0241408

Submitted: 30 September 2024 · Accepted: 30 November 2024 ·

Published Online: 23 December 2024



View Online



Export Citation



CrossMark

E. Nichelatti,^{1,a)} M. Piccinini,² A. Ampollini,² M. D. Astorino,² G. Bazzano,² P. Nenzi,² V. Surrenti,² E. Trinca,² and C. Ronsivalle²

AFFILIATIONS

¹Nuclear Department, ENEA C. R. Casaccia, Via Anguillarese 301, 00123 Rome, Italy

²Nuclear Department, ENEA C. R. Frascati, Via Enrico Fermi 45, 00044 Frascati (Rome), Italy

^{a)}Author to whom correspondence should be addressed: enrico.nichelatti@enea.it

ABSTRACT

In certain experimental setups used for proton irradiations at the TOP-IMPLART linear accelerator at the ENEA Frascati Center, the energy spectrum of the proton beam is measured at the end of a propagation path, which includes transmission through different materials, such as air, windows, slabs, etc. In this paper, we develop and test an approximate mathematical method to calculate the energy spectrum at the accelerator exit from such a measured transmitted spectrum. In the first experimental test application, the spectrum measurement exploits the visible photoluminescence of F_2 and F_3^+ color centers generated in lithium fluoride crystals by the interaction of the crystal lattice with protons. In the second test application, a simulated measurement of a propagated energy spectrum along a transport line is considered. In principle, the proposed method is applicable to the energy spectra of proton beams measured in any manner.

© 2024 Author(s). All article content, except where otherwise noted, is licensed under a Creative Commons Attribution-NonCommercial-NoDerivs 4.0 International (CC BY-NC-ND) license (<https://creativecommons.org/licenses/by-nc-nd/4.0/>). <https://doi.org/10.1063/5.0241408>

I. INTRODUCTION

TOP-IMPLART (Terapia Oncologica con Protoni—Intensity Modulated Proton Linear Accelerator for RadioTherapy) is a radio frequency (RF) pulsed linear accelerator (linac) originally developed at the ENEA Frascati Research Center as a prototype of a full linear accelerator for protontherapy. It is now evolving toward a facility available for research and industrial users in various fields of application. The system consists of a 425 MHz, 7 MeV injector—a 3 MeV RF quadrupole (RFQ) + a 7 MeV drift tube linac (DTL)—followed by a high frequency (3 GHz) booster composed of a sequence of eight side coupled DTL (SCDTL) accelerating modules. The proton beam can be accelerated to 63 or 71 MeV (other energy values can be achieved by suitable degraders) in 2.5 μ s pulses with a typical repetition rate of 25 Hz and a maximum pulse current of 20 μ A.

For accelerator-based experiments, particularly for medical applications such as proton therapy where beam energy directly translates to range penetration in the body, precise knowledge of the beam energy is essential. Different methods to measure the beam energy are used based on either destructive or non-destructive technique. The most common non-destructive technique is based on the use of spectrometers, which measure the

particle momentum by precisely determining the angle of deflection in a dipole magnetic field. Another non-destructive technique suitable for non-relativistic particles is the time of flight (TOF) method, which retrieves the particle velocity from the time it takes to travel between two fixed points whose distance is known.¹ Destructive, beam-intercepting techniques retrieve the energy from the study of the depth-dose distribution in a homogeneous reference material.

During commissioning of the TOP-IMPLART linac, a method employed to estimate the beam energy spectrum consisted of irradiating lithium fluoride (LiF) crystals at zero-angle grazing incidence and analyzing the luminescent Bragg curve formed by the emission of laser-active color centers² (CCs) generated in the material by the interaction with the accelerated protons.^{3–5} Indeed, ionizing radiation detectors based on the visible photoluminescence (PL) of aggregate F_2 and F_3^+ CCs in LiF crystals and thin films have gained a lot of interest in a wide range of applications—such as dosimetry,^{6–9} x-ray imaging,^{10,11} ion-track detection,^{12–16} and advanced diagnostics of proton beams^{4,17–23}—thanks to their peculiar characteristics, which include high transparency (14 eV bandgap), high intrinsic spatial resolution over a wide area, thermal

23 January 2025 10:32:22

stability, no development, or chemical treatment processing, handling in normal lighting conditions and response linearity up to dose values of $\sim 10^5$ – 10^6 Gy under proton irradiation.^{24,25}

On some occasions, e.g., to test the TOP-IMPLART proton beam for uniformity or to conduct specific experiments and irradiations, the LiF crystal is not positioned close to the linac exit, and a series of materials—such as windows, slabs, air, etc.—can be interposed between the accelerator exit and the crystal. In such cases, the LiF crystal records the information regarding an energy spectrum that is unavoidably modified by the propagation through those materials. While the result of this measurement is certainly of interest, estimating the proton-beam energy spectrum at the very exit of the linac is also valuable information, particularly for comparison with the spectrum calculated using a beam dynamics code. To this end, we present an approximate method to calculate the linac-exit energy spectrum of the proton beam from the energy spectrum at the measurement position.

II. MATERIALS AND METHODS

In the example experimental application of the proposed method (Sec. V), the proton irradiation was performed in air with the TOP-IMPLART linear RF accelerator²⁶ at a nominal exit energy of 35 MeV. The irradiated sample was a polished, commercially available LiF crystal by Mateck of dimensions $10 \times 10 \times 1$ mm³. Before irradiation, the crystal was pre-annealed at 500 °C for 2 h. The irradiation geometry was such that the proton beam impinged on one of the crystal's 1-mm thin sides at zero-angle grazing incidence, so that protons could propagate inside the LiF material until they stopped after having deposited all of their kinetic energy inside it. The irradiation dose amounted to 45 Gy at the LiF entry.

To obtain an estimation of the proton-beam spectrum at the LiF crystal position, the visible luminescent Bragg curve due the formation of F₂ and F₃⁺ CCs in the crystal was detected at 4× magnification using a Nikon Eclipse 80-i fluorescence microscope, equipped with a Hg lamp and an Andor Neo s-CMOS camera. The data were subsequently analyzed with a custom best-fit program coded in MATLAB,²⁷ which utilizes an analytical approximation of protons' Bragg curve in LiF⁴ and takes into account proton-beam fluence leakage through the crystal faces due to multiple Coulomb scattering.⁵

Monte Carlo simulations of energy spectrum propagation were conducted in FLUKA software^{28–30} (version 4–4.0) with its graphic interface Flair³¹ (version 3.3–1). In FLUKA, the PRECISIO physics parameters were used. Analytical evaluations of the functions t_μ and t_σ regulating the transmission of mean value and standard deviation of the energy spectrum, respectively, were obtained with the help of WOLFRAM MATHEMATICA.³² All the best-fitting curves were calculated in ORIGINLAB ORIGIN.³³ The LINAC software³⁴ was used for the beam dynamics simulation shown in Fig. 7.

III. THEORY

Let us assume that the energy spectrum $\phi_{\text{meas}}(E)$ of the proton beam of a linac was measured at a certain distance from the linac exit, E representing the energy coordinate at the measurement position. Knowing that a series of materials was interposed between

the linac exit and the measurement position, our purpose is that of estimating the energy spectrum $\phi_{\text{linac}}(E_0)$ at the linac exit. Here, E_0 is the energy coordinate at the linac exit.

Our method relies on the hypothesis that any perfectly monochromatic beam exiting the linac can be approximately represented by a Gaussian energy distribution at the measurement position. If the energy of the linac-exit monochromatic beam is E_0 , we define the mean energy and standard deviation of the Gaussian at the measurement position as $t_\mu(E_0)$ and $t_\sigma(E_0)$, respectively. Therefore, the energy spectrum at the measurement position is a superposition of such Gaussian distributions weighted by $\phi_{\text{linac}}(E_0)$, i.e.,

$$\phi_{\text{meas}}(E) = \int_0^\infty \phi_{\text{linac}}(E_0) G[E - t_\mu(E_0), t_\sigma(E_0)] dE_0, \quad (1)$$

where

$$G(x, w) = \frac{1}{\sqrt{2\pi} w} \exp\left(-\frac{x^2}{2w^2}\right). \quad (2)$$

By applying the variable substitution $E' = t_\mu(E_0)$, being $dE' = t'_\mu(E_0) dE_0$, Eq. (1) becomes

$$\phi_{\text{meas}}(E) = \int_0^\infty \frac{\phi_{\text{linac}}[t_\mu^{-1}(E')]}{t'_\mu[t_\mu^{-1}(E')]} G\left\{E - E', t_\sigma[t_\mu^{-1}(E')]\right\} dE', \quad (3)$$

where t'_μ is the derivative of t_μ .

Now, let us assume the Gaussian distribution to be narrow enough that the integral can be approximately evaluated using a second-order Taylor expansion of the integrand around E . As one can verify, the result is

$$\phi_{\text{meas}}(E) = \frac{\phi_{\text{linac}}[t_\mu^{-1}(E)]}{t'_\mu[t_\mu^{-1}(E)]} + \frac{t_\sigma^2[t_\mu^{-1}(E)]}{2} \frac{d^2}{dE^2} \left\{ \frac{\phi_{\text{linac}}[t_\mu^{-1}(E)]}{t'_\mu[t_\mu^{-1}(E)]} \right\}. \quad (4)$$

If the identities $E \equiv t_\mu(E_0)$, $E_0 \equiv t_\mu^{-1}(E)$, $d/dE \equiv [1/t'_\mu(E_0)] d/dE_0$ are taken into account and $t_\mu(E_0)$ is assumed to be enough well behaved that its derivatives with respect to E_0 of order higher than 1 can be neglected, after a few mathematical passages the following equation is obtained:

$$\phi_{\text{meas}}[t_\mu(E_0)] = \frac{\phi_{\text{linac}}(E_0)}{t'_\mu(E_0)} + \frac{1}{2} \frac{t_\sigma^2(E_0)}{[t'_\mu(E_0)]^3} \phi''_{\text{linac}}(E_0). \quad (5)$$

Equation (5) is a differential equation of order 2 in the unknown function $\phi_{\text{linac}}(E_0)$. Under the further assumption that the second term in the right-hand member can be considered much smaller than the others, the equation can be approximately

solved using the perturbation theory. To this purpose, let us write

$$\phi_{\text{linac}}(E_0) = \phi_{\text{linac}}^{(0)}(E_0) + \epsilon \phi_{\text{linac}}^{(1)}(E_0), \quad (6)$$

where ϵ is a small quantity of the same order of the second term in the right-hand member of Eq. (5). As usually done in the perturbation theory, ϵ will be set equal to 1 at the end of the process.

Therefore, substituting Eq. (6) into Eq. (5) and equating terms of the same order, one gets

$$\phi_{\text{linac}}^{(0)}(E_0) = t'_\mu(E_0) \phi_{\text{meas}}[t_\mu(E_0)], \quad (7)$$

$$\phi_{\text{linac}}^{(1)}(E_0) = -\frac{1}{2} \frac{t_\sigma^2(E_0)}{[t'_\mu(E_0)]^2} \frac{d^2}{dE_0^2} \left\{ t'_\mu(E_0) \phi_{\text{meas}}[t_\mu(E_0)] \right\}. \quad (8)$$

In this latter equation, calculating the right-hand member causes $t_\mu(E_0)$ derivatives of order higher than 1 to appear. As previously done, these are neglected under the hypothesis of enough well behaved $t_\mu(E_0)$. After a few passages, the following approximate expression for $\phi_{\text{linac}}^{(1)}(E_0)$ is obtained:

$$\phi_{\text{linac}}^{(1)}(E_0) = -\frac{1}{2} t_\sigma^2(E_0) t'_\mu(E_0) \phi''_{\text{meas}}[t_\mu(E_0)]. \quad (9)$$

Finally, setting $\epsilon \rightarrow 1$, the following first-order perturbative solution to Eq. (5) can be written:

$$\phi_{\text{linac}}(E_0) = t'_\mu(E_0) \left\{ \phi_{\text{meas}}[t_\mu(E_0)] - \frac{1}{2} t_\sigma^2(E_0) \phi''_{\text{meas}}[t_\mu(E_0)] \right\}. \quad (10)$$

According to this formula, the energy spectrum at the linac exit can be approximately calculated from the measured one by applying the energy domain substitution $E \rightarrow t_\mu(E_0)$ with a correction term—the one with $t_\sigma^2(E_0)$ —that accounts for energy spreading. The multiplication by $t'_\mu(E_0)$ is needed for approximate energy conservation, which becomes exact in case the energy spreading of monochromatic components can be neglected, i.e., when $t_\sigma(E_0) \rightarrow 0$. Indeed, if this is the case, Eq. (10) becomes

$$\phi_{\text{linac}}(E_0) dE_0 = \phi_{\text{meas}}(E) dE, \quad (11)$$

where $E = t_\mu(E_0)$ and $t'_\mu(E_0) = dE/dE_0$ have been used. Integration of Eq. (11) on both sides results in energy conservation.

As a final consideration, it should be pointed out that if low-energy components of $\phi_{\text{linac}}(E_0)$ are absorbed before reaching the position where $\phi_{\text{meas}}(E)$ is measured, they cannot be recovered by Eq. (10). Therefore, the above-commented energy conservation regards only the part of the spectrum that is transmitted without being absorbed.

IV. CALCULATION OF t_μ AND t_σ

We show two completely different methods to calculate $t_\mu(E_0)$ and $t_\sigma(E_0)$. The first method relies on analytical formulas for the propagation of the mean value and standard deviation of a Gaussian energy spectrum. The second method uses Monte Carlo

simulations to propagate a suitably chosen comb-shaped energy spectrum. We call them *analytical method* and *Monte Carlo method*, respectively.

A. Analytical method

In the Appendix of a recent paper, we provided analytical formulas for the propagation in a medium of the Gaussian energy spectrum of a proton beam.²² Those formulas, describing how mean value and standard deviation of the Gaussian change during propagation, were derived from Bragg-Kleeman's rule for proton range in matter and from a formula for range straggling, reported as Eq. (19) in a paper by Bortfeld.³⁵ We write here the above-mentioned formulas with a few modified symbols for better clarity. If z is the propagation distance inside a material, the changes in mean value and standard deviation of a Gaussian energy spectrum are described, respectively, by²²

$$\mu_{\text{out}} = \left(\mu_{\text{in}}^p - \frac{z}{\alpha} \right)^{1/p}, \quad (12)$$

$$\sigma_{\text{out}}^2 = \left(\alpha' \frac{\alpha p}{3p-2} \mu_{\text{in}}^p + \sigma_{\text{in}}^2 \right) \left(\frac{\mu_{\text{in}}}{\mu_{\text{out}}} \right)^{2p-2} - \alpha' \frac{\alpha p}{3p-2} \mu_{\text{out}}^p. \quad (13)$$

Here, α , p , and α' are characteristic parameters of the material,^{4,35} μ_{in} and σ_{in} are the energy mean value and standard deviation at the beginning of the propagation, while μ_{out} and σ_{out} are their corresponding values at the end of the propagation.

Knowing the sequence of materials that separate the spectrum measurement position from the linac exit, the above formulas can be readily used to evaluate $t_\mu(E_0)$ and $t_\sigma(E_0)$. Considering a monochromatic beam of energy E_0 exiting the linac, the mean energy μ_{out} and standard deviation σ_{out} at the exit of the first material crossed by the proton beam are calculated by setting $\mu_{\text{in}} = E_0$ and $\sigma_{\text{in}} = 0$ in Eqs. (12) and (13). The resulting μ_{out} and σ_{out} values can then be used in place of μ_{in} and σ_{in} to calculate propagation across the next material by applying again Eqs. (12) and (13). This process can be repeated in cascade for all the materials up to the exit of the last one, in correspondence of which one finally sets $t_\mu(E_0) = \mu_{\text{out}}$ and $t_\sigma(E_0) = \sigma_{\text{out}}$. This calculation can be conducted for any desired number of energies E_0 or even over the full energy domain by multiple function composition.

B. Monte Carlo method

Using Monte Carlo software, one can simulate the propagation of monochromatic beams through a sequence of materials that replicates the actual experimental setup. In particular, in FLUKA, a comb-shaped energy spectrum can be set at the source by means of the SPECSOUR and SPOTBEAM cards:²⁸ N monochromatic components E_i ($i = 1, 2, \dots, N$) of the spectral comb can be initialized and suitably spaced to obtain N conveniently separated transmitted components at the measurement position. Unless particular setups are considered, the shape of each of these transmitted components is approximately Gaussian, so that the transmitted energy spectrum can be best fitted with a Gaussian multi-peak function. The best fit

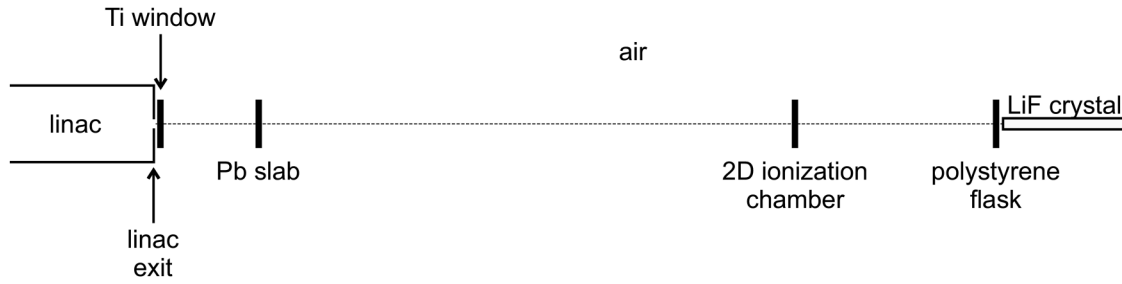


FIG. 1. Schematic representation (not to scale) of the setup considered for the example application of the developed theory.

result gives the values $t_{\mu}(E_i)$ and $t_{\sigma}(E_i)$ for each energy E_i of the comb.

V. FIRST EXAMPLE APPLICATION

According to the developed theory, the energy spectrum $\phi_{\text{linac}}(E_0)$ at the linac exit can be approximately calculated from the measured one, $\phi_{\text{meas}}(E)$, by applying Eq. (10). Here, we show an example application of the theory to an experimental case. It concerns the energy spectrum of the already mentioned TOP-IMPLART linac that was estimated for a cell irradiation experiment. The estimation was done by analyzing the Bragg curve extracted from the visible photoluminescent volume distribution of aggregate F_2 and F_3^+ CCs in a $10 \times 10 \times 1 \text{ mm}^3$ LiF crystal. These defects were generated in the LiF crystal lattice mainly by ionization induced by the proton beam, which impinged at zero-angle grazing incidence onto one of the thin 1-mm sides of the crystal. The nominal energy of the proton beam at the linac exit was 35 MeV, with an irradiation dose at the LiF entry of about 45 Gy.

This example application is representative of quite a complex setup due to the presence of several spaced materials in air with a resulting large distance between the linac exit and the LiF crystal.

A. Evaluation of t_{μ} and t_{σ}

The following sequence of materials was present between the linac exit and the LiF crystal (thickness between parentheses): Ti window ($50 \mu\text{m}$) \rightarrow air (22 cm) \rightarrow Pb slab ($210 \mu\text{m}$) \rightarrow air (120 cm) \rightarrow 2D ionization chamber ($170 \mu\text{m}$ H_2O -equivalent) \rightarrow air (45 cm) \rightarrow polystyrene flask (1.65 mm). The total mass thickness of this sequence amounts to about 0.678 g/cm^2 . The 1-mm thin side of the LiF crystal was placed in contact with the

polystyrene flask. A schematic representation (not to scale) of the setup is shown in Fig. 1. The values of the material parameters used in this example application, including mass density ρ , are listed in Table I. The values of p , α , and α' in this table were evaluated with the same method previously applied to LiF;⁴ here, however, FLUKA simulations were used, rather than SRIM³⁶ ones, to estimate proton ranges for energies up to 150 MeV. The values of the mass densities shown in Table I are those used by FLUKA.

The functions $t_{\mu}(E_0)$ and $t_{\sigma}(E_0)$ were evaluated for $E_0 = (33, 34, 35, 36, 37) \text{ MeV}$ by applying both the analytical and Monte Carlo methods illustrated in Secs. IV A and IV B. The transmitted spectrum at the LiF crystal position resulting from a Monte Carlo transport simulation (5×10^6 virtual protons in FLUKA) is shown in Fig. 2 together with its Gaussian multi-peak best fit. The parameters of this latter are listed in Table II.

The five $t_{\mu}(E_0)$ and $t_{\sigma}(E_0)$ points resulting from each of the two methods are plotted in Figs. 3 and 4. These figures report also the curves obtained by best fitting the data with the functions

$$t_{\mu}(E_0) = (E_0^P - Q)^{1/P}, \quad (14)$$

$$t_{\sigma}(E_0) = A \exp(-E_0/B) + C, \quad (15)$$

where P , Q , A , B , and C are fit parameters, whose optimal values are reported in Table III. Note how the form of the fitting function of $t_{\mu}(E_0)$ recalls that shown in Eq. (12), as if the whole propagation path could be considered as consisting of a single material. Indeed, this fact is due to the different values of p being mutually similar for all the involved materials, see Table I, thus allowing the functional form of Eq. (12) to be approximately maintained when the formula is applied in cascade.

TABLE I. Parameters of the materials between linac exit and the LiF crystal.

| material | p | α ($\mu\text{m}/\text{MeV}^p$) | α' ($10^{-6} \text{ MeV}^2/\mu\text{m}$) | ρ (g/cm^3) |
|----------------------|----------|---|---|-----------------------------------|
| Air | 1.788 21 | 19 119.8 | $1.022 79 \times 10^{-2}$ | $1.204 84 \times 10^{-3}$ |
| H_2O | 1.787 56 | 20.2399 | 8.721 50 | 1.0 |
| Pb | 1.679 31 | 6.326 28 | 70.5101 | 11.344 |
| Polystyrene | 1.794 13 | 19.0184 | 8.954 50 | 1.06 |
| Ti | 1.749 99 | 7.637 43 | 32.7630 | 4.5189 |

23 January 2025 10:32:22

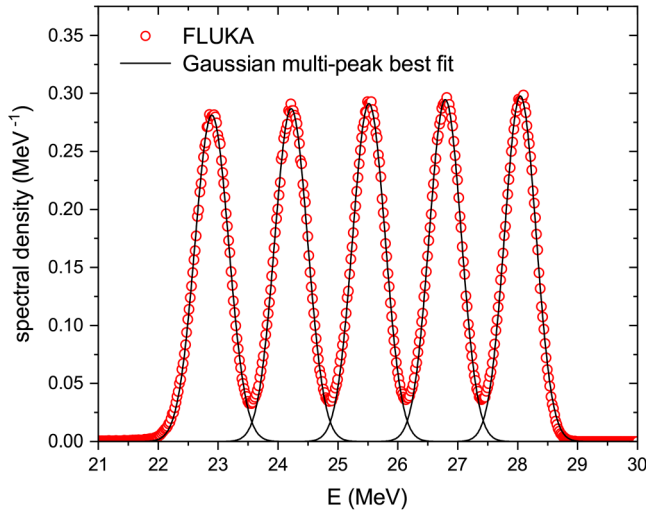


FIG. 2. Energy spectrum at the LiF crystal position resulting from the Monte Carlo (FLUKA) simulated transmission of the comb-shaped spectrum $E_0 = (33, 34, 35, 36, 37)$ MeV through the sequence of materials reported in the text and its Gaussian multi-peak best fit.

B. Bragg curve measurement and analysis

As already mentioned, proton-beam irradiation of LiF generates CCs in it, among which the aggregate F_2 and F_3^+ centers emit visible PL when optically excited in their almost overlapped absorption bands centered around the wavelength 450 nm. The photoluminescent volume distribution of such centers, created in the LiF crystal by the TOP-IMPLART proton beam, was detected in the fluorescence microscope by imaging the crystal 10×10 mm² top face. The image of the visible PL detected in this way is shown in Fig. 5—this figure shows also the irradiation and PL-image detection geometries. A more luminous vertical strip on the right side of the image is clearly visible—it corresponds to the Bragg peak. By integrating along the image vertical axis, the intensities of the pixels framed within the region of interest (yellow rectangle), a photoluminescent Bragg curve was obtained. The obtained Bragg curve is shown in Fig. 6, labeled as experimental, together with its best-fitting theoretical curve. This latter curve was calculated with a custom MATLAB code that utilizes an analytical approximate representation of Bragg curves in LiF⁴ and takes into account

TABLE II. Parameters of the Gaussian multi-peak best fit of Fig. 2. H is the height of each Gaussian component.

| E_0 (MeV) | H (MeV ⁻¹) | $t_{\mu}(E_0)$ (MeV) | $t_{\sigma}(E_0)$ (keV) |
|-------------|--------------------------|----------------------|-------------------------|
| 33 | 0.2812 ± 0.0005 | 22.8952 ± 0.0006 | 281.4 ± 0.6 |
| 34 | 0.2868 ± 0.0005 | 24.2193 ± 0.0006 | 274.2 ± 0.6 |
| 35 | 0.2912 ± 0.0005 | 25.5169 ± 0.0006 | 270.6 ± 0.6 |
| 36 | 0.2947 ± 0.0005 | 26.7913 ± 0.0006 | 267.6 ± 0.6 |
| 37 | 0.2977 ± 0.0005 | 28.0440 ± 0.0005 | 261.7 ± 0.5 |

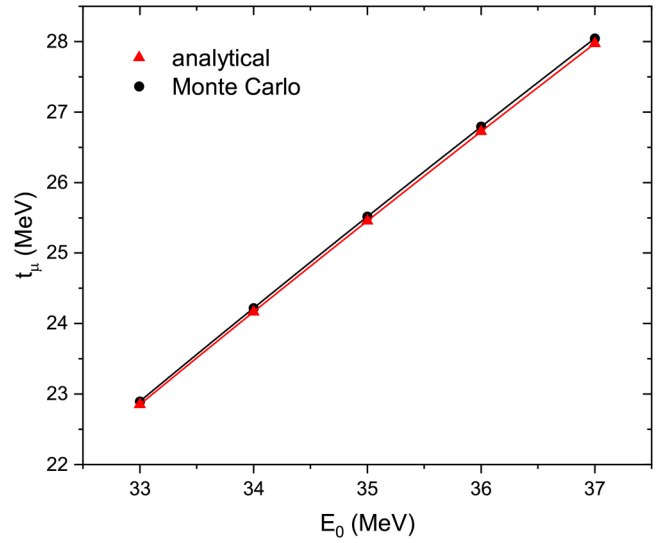


FIG. 3. Values of the function $t_{\mu}(E_0)$ calculated at (33, 34, 35, 36, 37) MeV using the two methods illustrated in Secs. IV A and IV B (points). The best fitting curves found using Eq. (14) are also shown (solid lines).

proton-beam fluence leakage through the crystal faces due to multiple Coulomb scattering.⁵ In the best fit, a single-band Gaussian energy spectrum was assumed, for which these optimal parameter values were found: mean value of (25.55 ± 0.17) MeV and standard deviation of (455 ± 15) keV.

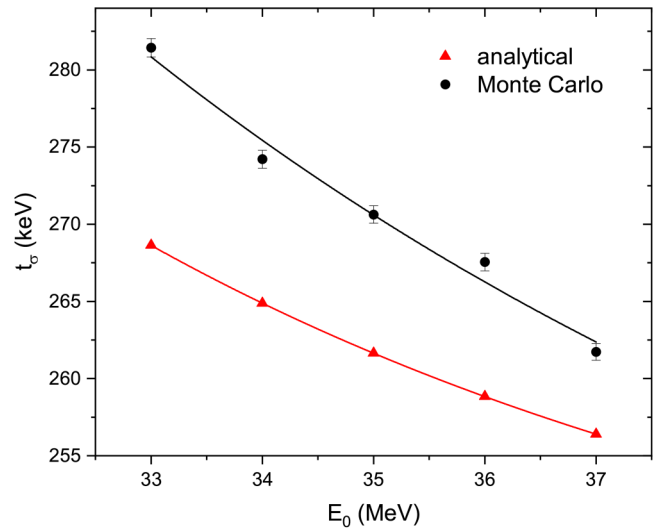


FIG. 4. Values of the function $t_{\sigma}(E_0)$ calculated at (33, 34, 35, 36, 37) MeV using the two methods illustrated in Secs. IV A and IV B (points). The best fitting curves found using Eq. (15) are also shown (solid lines).

23 January 2025 10:32:22

TABLE III. Fit parameters of $t_\mu(E_0)$ and $t_\sigma(E_0)$ (Figs. 3 and 4) as defined in Eqs. (14) and (15).

| Method | P | Q (MeV ²) | A (MeV) | B (MeV) | C (MeV) |
|-------------|-----------------------|-------------------------|--------------|-------------------|---------------------|
| Analytical | 1.76521 ± 0.00001 | 40.7436 ± 0.0001 | 111 ± 63 | 1.188 ± 0.091 | 0.1077 ± 0.0013 |
| Monte Carlo | 1.7634 ± 0.0024 | 41.12 ± 0.26 | 83 ± 48 | 1.25 ± 0.10 | 0.1091 ± 0.0013 |

C. Backpropagation of the measured energy spectrum

The Gaussian energy spectrum found in Sec. V B is assumed to be the measured one, $\phi_{\text{meas}}(E)$. According to the developed theory, it can be propagated back to the linac exit using Eq. (10), with the functions $t_\mu(E_0)$ and $t_\sigma(E_0)$ evaluated in Sec. V A. This operation, performed with a custom code programmed in MATHEMATICA, gave the results shown in Fig. 7. Note in the figure that the two methods of calculation of $t_\mu(E_0)$ and $t_\sigma(E_0)$, the analytical one (Sec. IV A) and the Monte Carlo one (Sec. IV B), lead to slightly mutually shifted distributions $\phi_{\text{linac}}(E_0)$ due to the quite different approaches the two methods utilize. However, the difference between the two calculated $\phi_{\text{linac}}(E_0)$ is almost negligible, as witnessed by the value of the parameters of the Gaussian best fits of these curves reported in Table IV.

Regarding the approximately 1.5% difference in Fig. 7 between the standard deviations obtained with the two methods as compared with that of about 3% in Fig. 4, which could look like a contradiction, it should be stressed that Figs. 4 and 7 concern different spectral sources and positions in the setup. Indeed, the data in Fig. 4 are energy spreads at the measurement distance calculated from monochromatic beams at the linac exit; on the other hand, the curves in Fig. 7 are spectra at linac exit calculated from a non-monochromatic spectrum at the measurement distance.

A more significant difference is visible in Fig. 7 between the energy spectrum simulated using beam dynamics code³⁴ and the above-mentioned pair of backpropagated $\phi_{\text{linac}}(E_0)$. In addition to the difference in height, simply due to unitary area normalization, the most important difference regards the width of this

distribution. This fact is quantified by observing the standard deviations in Table IV, which also reports the Gaussian best-fitting parameters of the beam-dynamics spectrum. The larger widths of the two backpropagated $\phi_{\text{linac}}(E_0)$ with respect to the beam dynamics simulation are probably only in part due to a tendency of the model to slightly overestimate the energy spread, as we will discuss in Sec. IV B and in the Conclusions. Indeed, when propagated with FLUKA up to the LiF crystal position, these two backpropagated $\phi_{\text{linac}}(E_0)$ agree quite well with the measured energy spectrum, as later shown in Sec. V D. Instead, such a difference can presumably be ascribed to some discrepancies between the *ideal* operating conditions as modeled in the start-to-end beam dynamics simulation and the real conditions.

As a matter of fact, the energy spectrum in Fig. 7 resulting from beam dynamics calculations was computed for an ideal beam in the absence of errors, with a perfect field, and no jitter in field amplitude and phase. For this reason, the obtained energy spread must be regarded as a lower limit, because errors in electric field amplitude and phase in the injector and in the accelerating modules of the booster can increase the proton energy spread at the linac output compared to the design value. A detailed description of the accelerator, including all the main design parameters and beam dynamics, is reported in another paper.²⁶ In it, the results of an error analysis are also included that focus on setting accuracy limits for the machine parameters that affect the characteristics of the output beam. Another significant point to consider is that the start-to-end computation starts from the injector output rather than the source. The 7 MeV injector is a commercial

23 January 2025 10:32:22

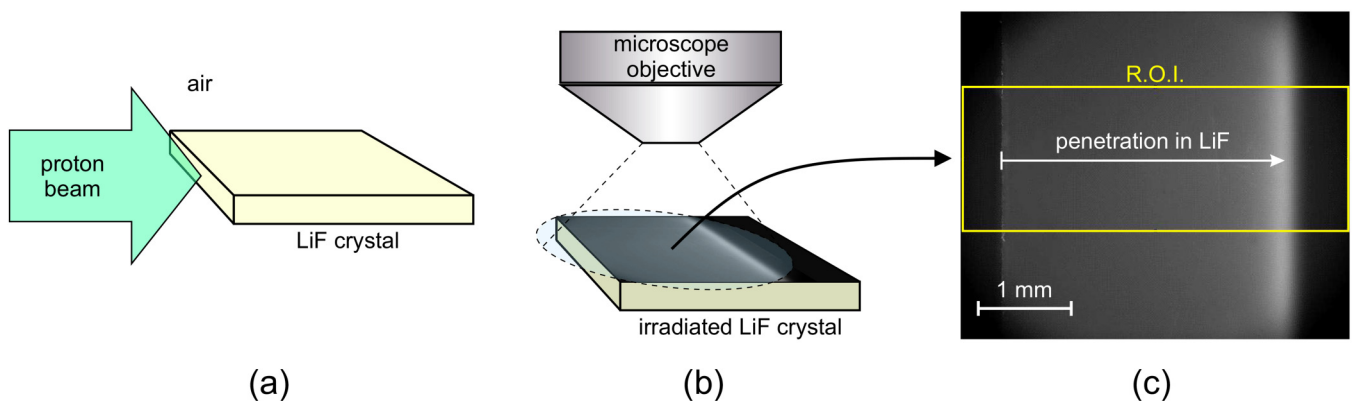


FIG. 5. Schemes (not to scale) of (a) proton irradiation of the LiF crystal and (b) subsequent PL-image detection at the fluorescence microscope; (c) experimental PL-image detected at the fluorescence microscope. The Bragg curve in Fig. 6 was obtained by integrating along the image vertical axis the pixel intensities within the region of interest (ROI) in (c).

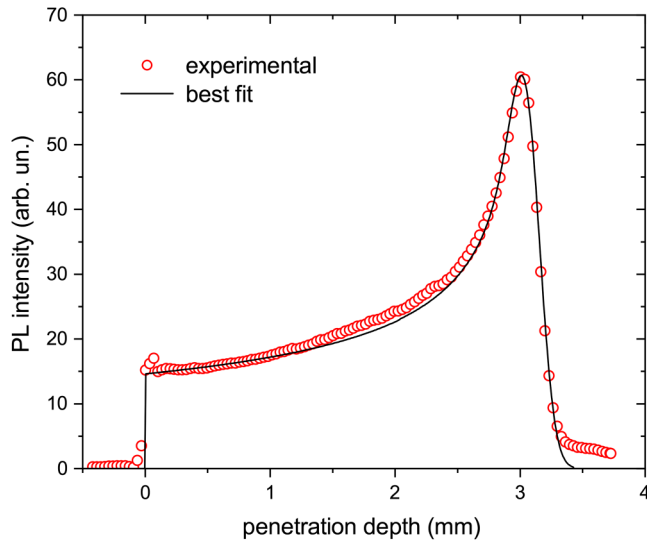


FIG. 6. Experimental photoluminescent Bragg curve in the LiF crystal and its best fit. The experimental curve was extracted from the region of interest in Fig. 5(c).

machine (ACCSYS-Hitachi PL7 model), while the following high-frequency structures of the booster were designed by ENEA and are included in the code with a detailed model. In the absence of an injector model, the LINAC code calculations use as input for the particles' coordinates the phase-space longitudinal and transverse

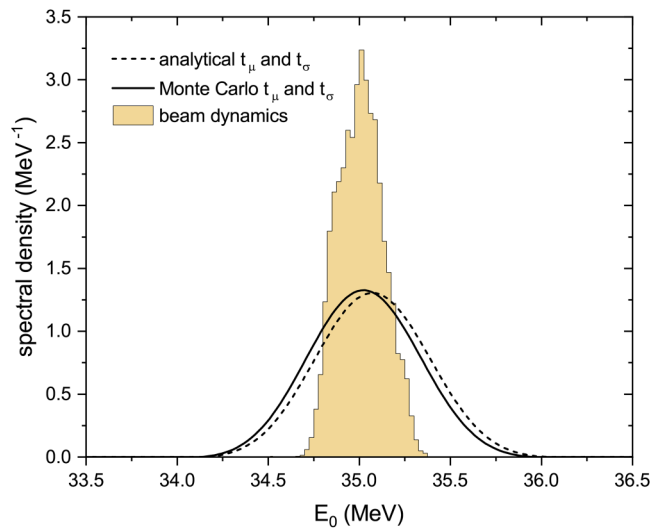


FIG. 7. Backpropagated $\phi_{\text{linac}}(E_0)$ obtained by applying Eq. (10) to $\phi_{\text{meas}}(E)$ with the functions $t_\mu(E_0)$ and $t_\sigma(E_0)$ evaluated with the analytical (Fig. 3) and Monte Carlo (Fig. 4) methods. For comparison, the energy spectrum simulated using beam dynamics LINAC software is also shown.

TABLE IV. Gaussian fit parameters of the backpropagated spectra in Fig. 7.

| Spectrum | Mean value (MeV) | Standard deviation (keV) |
|------------------------------------|----------------------|--------------------------|
| Analytical t_μ and t_σ | 35.0734 ± 0.0004 | 306.9 ± 0.4 |
| Monte Carlo t_μ and t_σ | 35.0250 ± 0.0005 | 302.3 ± 0.5 |
| Beam dynamics | 35.004 ± 0.003 | 133 ± 3 |

parameters given by the injector manufacturer, which might not accurately describe the actual injector output beam in all operating conditions.

These considerations could largely justify the difference between the beam dynamics spectrum and the backpropagated ones, which, however, is also partly ascribable to a slight overestimation of the width of the backpropagated spectra, as already mentioned and later discussed in Sec. VI B and in the Conclusions. Nonetheless, the almost perfect matching of the Gaussian peak positions of the three spectra in Fig. 7, quantified by the Gaussian mean values in Table IV, is quite comforting. Indeed, the largest difference among them amounts to $\sim 0.2\%$.

D. Check of the backpropagated energy spectra

To check how well (or not well) the developed theory works for this example application, the two backpropagated energy spectra $\phi_{\text{linac}}(E_0)$, calculated with the methods illustrated in Secs. IV A and IV B, were propagated up to the LiF crystal position along the experimental path of Fig. 1 in two distinct FLUKA simulations using 5×10^6 virtual protons. Another propagation in FLUKA with the same parameters was simulated for the beam-dynamics

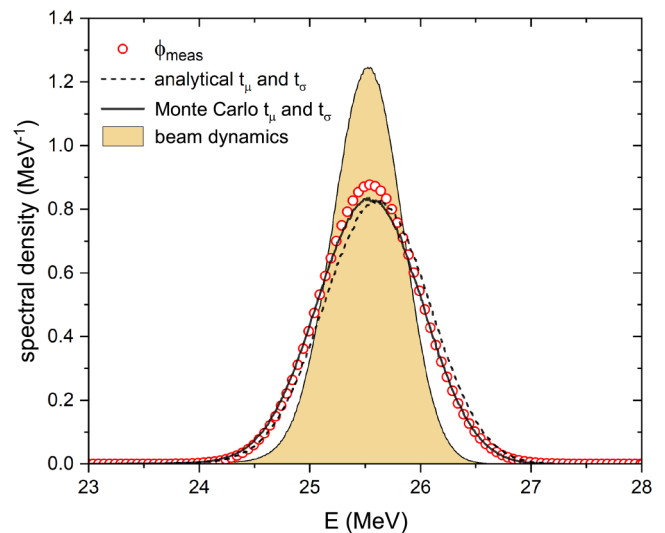


FIG. 8. FLUKA simulated propagation along the path of Fig. 1 of the three energy spectra of Fig. 7 and their comparison with $\phi_{\text{meas}}(E)$ that was experimentally found by best fitting the Bragg curve of Fig. 6.

23 January 2025 10:32:22

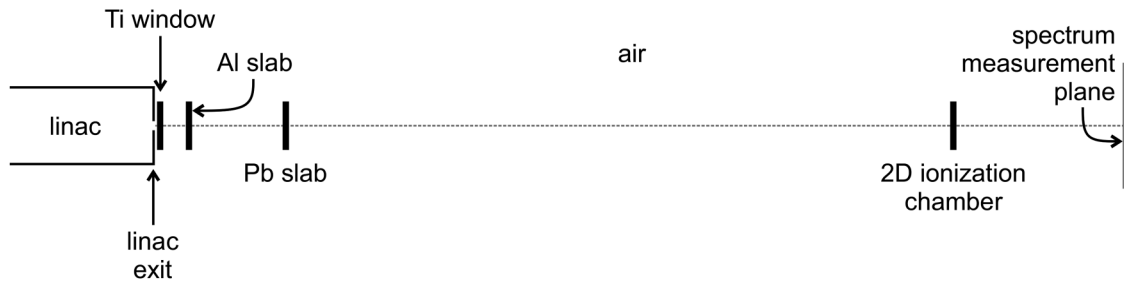


FIG. 9. Schematic representation (not to scale) of the setup considered for the second example application of the developed theory.

spectrum of Fig. 7. Finally, the propagated spectra resulting from the above three simulations were compared with the measured spectrum $\phi_{\text{meas}}(E)$. The comparison is shown in Fig. 8, while the corresponding numerical values of the Gaussian best fits of the four spectra are reported in Table V—the ones regarding the experimental case are those derived from the best fit of the Bragg curve discussed in Sec. V B.

In addition to the smaller width of the propagated beam-dynamics spectrum, clearly caused by its smaller width at the linac exit, one notices that the other two propagated spectra match the experimental one fairly well, just with some minor differences. The first minor difference is a slightly smaller height of these two propagated spectra with respect to $\phi_{\text{meas}}(E)$, which is ascribable to a slight overestimation of their standard deviations by less than 5%. The other minor difference regards only the spectrum which was backpropagated using analytically evaluated $t_{\mu}(E_0)$ and $t_{\sigma}(E_0)$ —dashed-line curve in Fig. 8—whose peak energy is larger by about 50 keV than that of the experimental spectrum, i.e., less than 0.2% larger. Considering the several approximations and assumptions made in developing our theory, it can be concluded that it worked surprisingly well for the present example.

It is worth pointing out that, even though in this example we made large use of Monte Carlo simulations to gain a more confident view on the obtained results, one could have operated just using analytical calculations, as the good results obtained with the analytical method witness. Additionally, even the final check of spectrum propagation from the linac exit up to the LiF crystal position could have been conducted by analytical means. As a matter of fact, using Eqs. (12) and (13) for the propagation of the linac-exit spectrum to the LiF crystal position, one gets Gaussian spectra with mean value of 25.55 MeV and standard deviation of 471 keV for

the case of analytically evaluated $t_{\mu}(E_0)$ and $t_{\sigma}(E_0)$, and mean value of 25.55 MeV and standard deviation of 467 keV for the case of Monte Carlo evaluated $t_{\mu}(E_0)$ and $t_{\sigma}(E_0)$. These values very well compare with those in Table V, suggesting that Eqs. (12) and (13) are quite reliable for the propagation of Gaussian-shaped energy spectra even in the presence of several materials.

VI. SECOND EXAMPLE APPLICATION

Here, we report another example of application of our back-propagation method. This time, we consider a Monte Carlo simulated measurement of the energy spectrum to directly compare the backpropagated spectra with a known spectrum at the linac exit. A collimated beam with a Gaussian energy distribution, with a mean value of 55.5 MeV and standard deviation of 210 keV, is assumed to be emitted from a proton linac. These values were obtained from a beam dynamics simulation of the TOP-IMPLART linac

TABLE V. Gaussian fit parameters of the spectra in Fig. 8.

| Spectrum | Mean value (MeV) | Standard deviation (keV) |
|--|----------------------|--------------------------|
| Experimental (ϕ_{meas}) | 25.55 ± 0.17 | 455 ± 15 |
| Analytical t_{μ} and t_{σ} | 25.6043 ± 0.0002 | 476.0 ± 0.2 |
| Monte Carlo t_{μ} and t_{σ} | 25.5379 ± 0.0002 | 471.5 ± 0.2 |
| Beam dynamics | 25.5189 ± 0.0002 | 315.0 ± 0.2 |

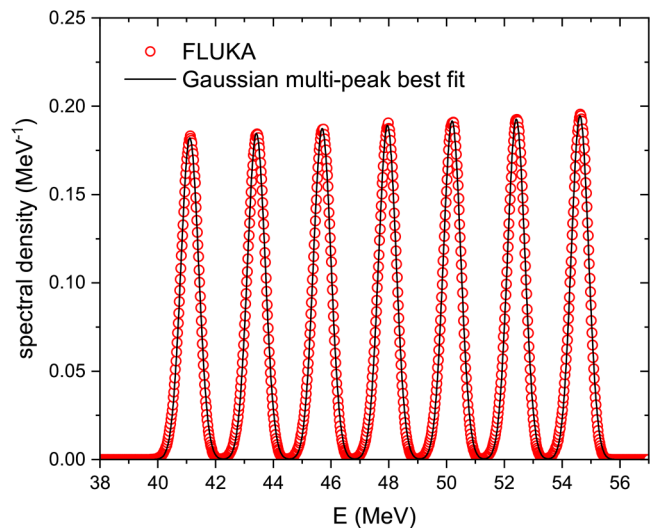


FIG. 10. Energy spectrum at the spectrum measurement plane resulting from the Monte Carlo (FLUKA) simulated transmission of the comb-shaped spectrum $E_0 = (50, 52, 54, 56, 58, 60, 62)$ MeV through the sequence of materials reported in the text and its Gaussian multi-peak best fit.

23 January 2025 10:32:22

TABLE VI. Parameters of the Gaussian multi-peak best fit of Fig. 10. H is the height of each Gaussian component.

| E_0 (MeV) | H (MeV ⁻¹) | $t_\mu(E_0)$ (MeV) | $t_\sigma(E_0)$ (keV) |
|-------------|--------------------------|--------------------|-----------------------|
| 50 | 0.1820 ± 0.0006 | 41.110 ± 0.001 | 306 ± 1 |
| 52 | 0.1846 ± 0.0006 | 43.415 ± 0.001 | 304 ± 1 |
| 54 | 0.1873 ± 0.0006 | 45.694 ± 0.001 | 302 ± 1 |
| 56 | 0.1892 ± 0.0006 | 47.952 ± 0.001 | 301 ± 1 |
| 58 | 0.1916 ± 0.0006 | 50.190 ± 0.001 | 300 ± 1 |
| 60 | 0.1927 ± 0.0006 | 52.411 ± 0.001 | 299 ± 1 |
| 62 | 0.1946 ± 0.0006 | 54.618 ± 0.001 | 298 ± 1 |

performed with LINAC software. In the simulation of the propagated spectrum measurement performed in FLUKA, the beam is transported to a spectrum measurement plane through a sequence of materials, as shown in Fig. 9. The transport line depicted in this figure replicates that of an actual experimental setup, in which the beam is spatially enlarged by exploiting the scattering caused by passing through the lead slab to perform cell radiobiology experiments at the distance where the spectrum measurement plane is located. At this distance, the flux of the beam is uniform within an area of several square centimeters.

Starting from the linac exit, the sequence of materials before the spectrum measurement plane in the simulated transport line is as follows (thickness between parentheses): Ti window (50 μm) → air (2 cm) → Al slab (500 μm) → air (17.5 cm) → Pb slab (600 μm) → air (158 cm) → 2D ionization chamber (170 μm H₂O-equivalent) → air (25 cm). For the parameters of these

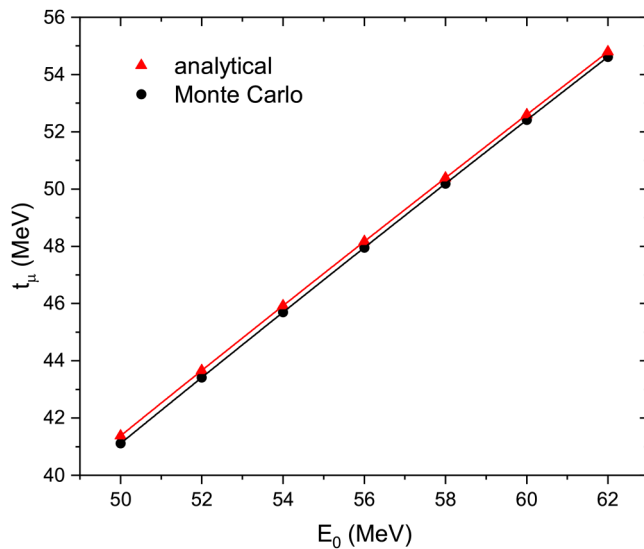


FIG. 11. Values of the function $t_\mu(E_0)$ calculated at (50, 52, 54, 56, 58, 60, 62) MeV using the two methods illustrated in Secs. IV A and IV B (points). The best fitting curves found using Eq. (14) are also shown (solid lines).

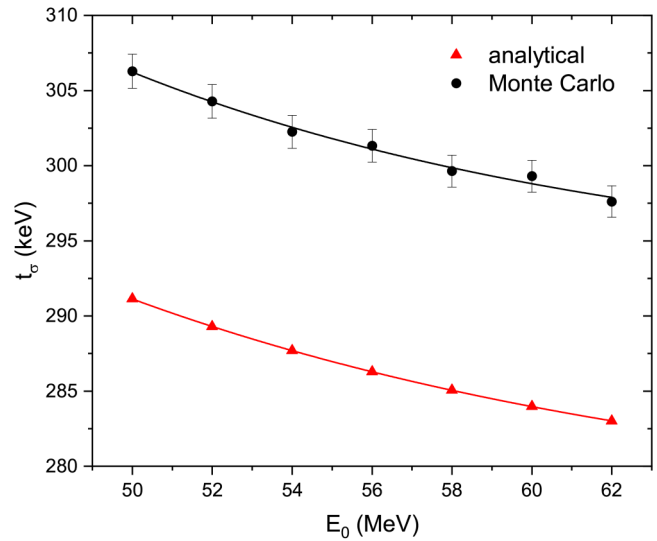


FIG. 12. Values of the function $t_\sigma(E_0)$ calculated at (50, 52, 54, 56, 58, 60, 62) MeV using the two methods illustrated in Secs. IV A and IV B (points). The best fitting curves found using Eq. (15) are also shown (solid lines).

materials, we used the values reported in Table I, and for aluminum—not present in that table—we used the following values: $p = 1.76322$, $\alpha = 10.9118 \mu\text{m}/\text{MeV}^2$, $\alpha' = 20.4350 \times 10^{-6} \text{MeV}^2/\mu\text{m}$, $\rho = 2.699 \text{g}/\text{cm}^3$. The first three parameters were evaluated with the same method used for LiF,⁴ but running FLUKA simulations instead of SRIM ones. The value of the mass density is the one used by FLUKA. The total mass thickness of this transport line is about 1.116 g/cm², which is almost twice that of the experimental example reported in Sec. V. In view of this significantly larger value, this test represents a more challenging case to tackle with our approximate approach.

A. Evaluation of t_μ and t_σ

The functions $t_\mu(E_0)$ and $t_\sigma(E_0)$ were evaluated for $E_0 = (50, 52, 54, 56, 58, 60, 62)$ MeV using the analytical and Monte Carlo methods discussed in Secs. IV A and IV B. The propagated spectrum at the spectrum measurement plane resulting from a Monte Carlo transport simulation (2.5×10^7 virtual protons in FLUKA) is shown in Fig. 10 together with its Gaussian multi-peak best fit. The parameters of the latter are listed in Table VI.

The seven $t_\mu(E_0)$ and $t_\sigma(E_0)$ points resulting from each of the two methods are plotted in Figs. 11 and 12. In these figures, the curves obtained by best fitting the data with Eqs. (14) and (15) are also shown. The optimal values of the parameters of these fits are listed in Table VII. The large uncertainty associated with parameter A for the Monte Carlo method has not impacted the fairly good result shown in the following.

23 January 2025 10:32:22

TABLE VII. Fit parameters of $t_\mu(E_0)$ and $t_\sigma(E_0)$ (Figs. 11 and 12) as defined in Eqs. (14) and (15).

| Method | P | Q (MeV ^{P}) | A (MeV) | B (MeV) | C (MeV) |
|-------------|-----------------------|--------------------------------------|---------------|------------------|-----------------|
| Analytical | 1.73091 ± 0.00007 | 243.78 ± 0.08 | 397 ± 15 | 15.23 ± 0.23 | 276.3 ± 0.2 |
| Monte Carlo | 1.7521 ± 0.0003 | 275.1 ± 0.4 | 666 ± 840 | 12.9 ± 4.9 | 292 ± 3 |

B. Forward and backpropagation of the energy spectrum

In a FLUKA simulation, the energy spectrum was propagated from the linac exit to the spectrum measurement plane through the transport line depicted in Fig. 9. For this simulation, 2.5×10^7 virtual protons were launched. The propagated spectrum was approximately Gaussian. Then, using the developed theory, this propagated spectrum was backpropagated using Eq. (10) and the functions $t_\mu(E_0)$ and $t_\sigma(E_0)$, whose parameter values are listed in Table VII and correspond to the two methods discussed in Secs. IV A and IV B. These backpropagated spectra were also approximately Gaussian. The results of this forth-and-back process are reported in Fig. 13 and Table VIII.

It can be noticed that the backpropagated spectrum obtained using the Monte Carlo deduced $t_\mu(E_0)$ and $t_\sigma(E_0)$ overlaps better with the starting linac-exit spectrum than the one obtained using the analytically deduced $t_\mu(E_0)$ and $t_\sigma(E_0)$. However, for the latter, the mean energy differs from that of the linac-exit spectrum by only 0.36%, which is quite an acceptable error considering all the involved approximations.

As for the slightly larger standard deviations found with both methods, we can attribute this overestimation to truncating the

Taylor expansion of the integrand in Eq. (3) to the second order. Indeed, as already pointed out when commenting on Eq. (10), the second order of this Taylor expansion determines the spreading of the energy spectrum. Higher orders beyond the second one would allow refining the energy spread evaluation. Not considering them is an approximation whose influence can become more significant in cases where the mass thickness of the transport line is larger, as in the present example. Nonetheless, using the second-order approximation, both the approaches of Secs. IV A and IV B have provided acceptable, although not ideal, estimations of the energy spectrum at the linac exit for this example.

VII. CONCLUSIONS

The theory presented in this paper has been developed to retrieve the energy spectrum of a proton beam exiting from a linac using a measurement taken at a certain distance. Along the propagation path from the linac exit to the measurement position, a series of materials—such as windows, slabs, air, etc.—can be present. To apply the theory, either Monte Carlo propagation simulations of a suitable comb of monochromatic energies or knowledge of the material parameters p , α , and α' must be available—this allows evaluating the functions t_μ and t_σ on which our approach relies.

The presented method is clearly an approximate one due to the several assumptions that were made and the perturbative approach utilized to solve a differential equation. From the reported examples, it seems that the method succeeds in estimating the peak energy with good precision, but that it tends to slightly overestimate the width of the backpropagated spectra, as also found for another test case not reported here for space reasons. As commented in Sec. VI B, this is presumably ascribable to having truncated the integrand function in Eq. (1) to the second order of its Taylor expansion. Unfortunately, retaining higher-order terms would lead to an unmanageable higher-order differential equation in place of Eq. (5).

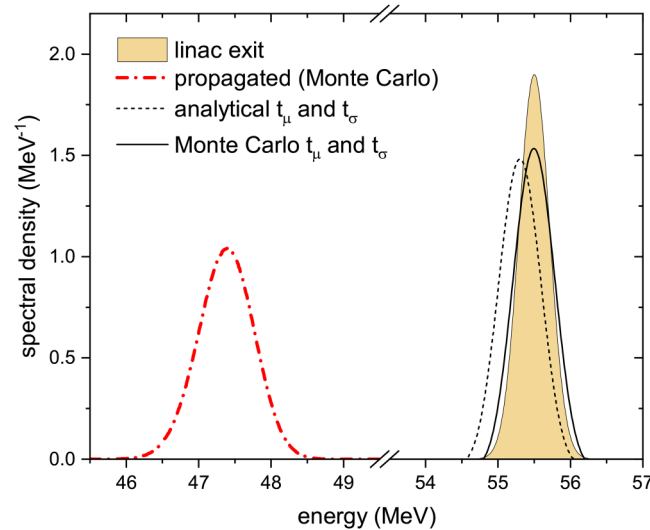


FIG. 13. Test Gaussian energy spectrum set at the linac exit with its FLUKA simulated propagation along the path of Fig. 9, and backpropagated spectra estimated using Eq. (10) and the functions $t_\mu(E_0)$ and $t_\sigma(E_0)$ deduced by best fitting the data obtained using the two methods discussed in Secs. IV A and IV B.

TABLE VIII. Gaussian fit parameters of the spectra in Fig. 13.

| Spectrum | Mean value (MeV) | Standard deviation (keV) |
|------------------------------------|----------------------|--------------------------|
| Linac exit | 55.5 | 210 |
| Propagated (Monte Carlo) | 47.3841 ± 0.0003 | 383.4 ± 0.3 |
| Analytical t_μ and t_σ | 55.3019 ± 0.0007 | 273.8 ± 0.7 |
| Monte Carlo t_μ and t_σ | 55.4959 ± 0.0008 | 266.0 ± 0.8 |

23 January 2025 10:32:22

Despite these facts, the discussed example applications have provided acceptable quantitative results in the presence of quite complex transport lines from the linac exit to the measurement position. The method's precision is likely to decrease with increasing mass thickness of the transport line due to increasing sources of energy spreading. The precision level might become even lower when the approach based on Eqs. (12) and (13) is used because these equations were derived using approximate formulas for the penetration range and range straggling.^{22,35} Nonetheless, settling for an approximate result, the proposed method can, in principle, be applied entirely analytically for a quick evaluation without resorting to Monte Carlo simulations. As already mentioned above, in such a case, the values of the parameters p , α and α' for the involved materials need to be known.

The method has been tested on example cases based on experimental beam delivery lines used for target irradiations with the proton beam of the TOP-IMPLART linear accelerator in operation at the ENEA Frascati Center.

ACKNOWLEDGMENTS

This research has been carried on within the TOP-IMPLART (Oncological Therapy with Protons—Intensity Modulated Proton Linear Accelerator for Radiotherapy) Project, funded by Regione Lazio, Italy.

AUTHOR DECLARATIONS

Conflict of Interest

The authors have no conflicts to disclose.

Author Contributions

E. Nichelatti: Conceptualization (lead); Data curation (equal); Formal analysis (equal); Investigation (supporting); Methodology (equal); Resources (equal); Software (lead); Supervision (equal); Validation (equal); Visualization (lead); Writing – original draft (lead); Writing – review & editing (lead). **M. Piccinini:** Data curation (equal); Formal analysis (equal); Investigation (lead); Methodology (equal); Resources (equal); Validation (equal); Writing – original draft (equal); Writing – review & editing (equal). **A. Ampollini:** Investigation (equal); Resources (equal); Writing – review & editing (supporting). **M. D. Astorino:** Investigation (equal); Resources (equal); Writing – review & editing (equal). **G. Bazzano:** Investigation (equal); Resources (equal); Writing – review & editing (equal). **P. Nenzi:** Funding acquisition (lead); Investigation (equal); Project administration (lead); Resources (equal); Writing – review & editing (supporting). **V. Surrenti:** Investigation (equal); Resources (equal); Writing – review & editing (supporting). **E. Trinca:** Investigation (equal); Resources (equal); Writing – review & editing (supporting). **C. Ronsivalle:** Conceptualization (supporting); Formal analysis (equal); Investigation (lead); Resources (lead); Software (lead); Supervision (lead); Validation (equal); Visualization (supporting); Writing – original draft (equal); Writing – review & editing (equal).

DATA AVAILABILITY

The data that support the findings of this study are available from the corresponding author upon reasonable request.

REFERENCES

- ¹F. Galizzi, M. Caldara, and A. Jef, “A time-of-flight based energy measurement system for the LIGHT medical accelerator,” *J. Phys.: Conf. Ser.* **1067**, 072019 (2018).
- ²W. B. Fowler, *Physics of Color Centers* (Academic Press, New York, 1968).
- ³E. Nichelatti, M. Piccinini, A. Ampollini, L. Picardi, C. Ronsivalle, F. Bonfigli, M. A. Vincenti, and R. M. Montereali, “Bragg-curve imaging of 7 MeV protons in a lithium fluoride crystal by fluorescence microscopy of colour centres,” *Europhys. Lett.* **120**, 56003 (2017).
- ⁴E. Nichelatti, C. Ronsivalle, M. Piccinini, L. Picardi, and R. M. Montereali, “An analytical approximation of proton Bragg curves in lithium fluoride for beam energy distribution analysis,” *Nucl. Instrum. Methods Phys. Res. B* **446**, 29–36 (2019).
- ⁵E. Nichelatti, M. Piccinini, P. Nenzi, L. Picardi, C. Ronsivalle, and R. M. Montereali, “Proton-beam energy diagnostics by color-center photoluminescence imaging in LiF crystals: Implementation of multiple Coulomb scattering into an analytical Bragg-curve model,” *Nucl. Instrum. Methods Phys. Res. B* **547**, 165207 (2024).
- ⁶W. L. McLaughlin, “Colour centres in LiF for measurement of absorbed doses up to 100 MGy,” *Radiat. Prot. Dosimetry* **66**, 197–200 (1996).
- ⁷W. L. McLaughlin, J. M. Puhl, A. Kovács, M. Baranyai, I. Slezsák, M. C. Saylor, S. A. Saylor, S. D. Miller, and M. Murphy, “Sunna dosimeter: An integrating photoluminescent film and reader system; work in progress,” *Radiat. Phys. Chem.* **55**, 767–771 (1999).
- ⁸J. E. Villarreal-Barajas, M. Piccinini, M. A. Vincenti, F. Bonfigli, R. F. Khan, and R. M. Montereali, “Visible photoluminescence of color centers in LiF crystals for absorbed dose evaluation in clinical dosimetry,” *IOP Conf. Ser.: Mater. Sci. Eng.* **80**, 012020 (2015).
- ⁹M. Piccinini, E. Nichelatti, M. Pimpinella, V. De Coste, and R. M. Montereali, “Dose response of visible color center radiophotoluminescence in lithium fluoride crystals irradiated with a reference ⁶⁰Co gamma beam in the 1–20 Gy dose range,” *Radiat. Meas.* **151**, 106705 (2022).
- ¹⁰G. Baldacchini, F. Bonfigli, F. Flora, R. M. Montereali, D. Murra, E. Nichelatti, A. Faenov, and T. Pikuz, “High-contrast photoluminescent patterns in lithium fluoride crystals produced by soft x-rays from a laser-plasma source,” *Appl. Phys. Lett.* **80**, 4810–4812 (2002).
- ¹¹G. Baldacchini, F. Bonfigli, A. Faenov, F. Flora, R. Montereali, A. Pace, T. Pikuz, and L. Reale, “Lithium fluoride as a novel x-ray image detector for biological μ -world capture,” *J. Nanosci. Nanotechnol.* **3**, 483–486 (2003).
- ¹²P. Bilski and B. Marczevska, “Fluorescent detection of single tracks of alpha particles using lithium fluoride crystals,” *Nucl. Instrum. Methods Phys. Res. B* **392**, 41–45 (2017).
- ¹³P. Bilski, B. Marczevska, W. Gieszczyk, M. Kłosowski, T. Nowak, and M. Naruszewicz, “Lithium fluoride crystals as fluorescent nuclear track detectors,” *Radiat. Prot. Dosim.* **178**, 337–340 (2018).
- ¹⁴P. Bilski, B. Marczevska, W. Gieszczyk, M. Kłosowski, M. Naruszewicz, M. Sankowska, and S. Kodaira, “Fluorescent imaging of heavy charged particle tracks with LiF single crystals,” *J. Lumin.* **213**, 82–87 (2019).
- ¹⁵M. Sankowska, P. Bilski, and B. Marczevska, “Thermal enhancement of the intensity of fluorescent nuclear tracks in lithium fluoride crystals,” *Radiat. Meas.* **157**, 106845 (2022).
- ¹⁶M. Piccinini, E. Nichelatti, G. Esposito, E. Cisbani, F. Santavenere, P. Anello, V. Nigro, M. A. Vincenti, F. Limosani, C. Ronsivalle, A. Ampollini, C. De Angelis, and R. M. Montereali, “Detection of fluorescent low-energy proton tracks in lithium fluoride crystals,” *Radiat. Meas.* **174**, 107140 (2024).
- ¹⁷M. Piccinini, F. Ambrosini, A. Ampollini, M. Carpanese, L. Picardi, C. Ronsivalle, F. Bonfigli, S. Libera, M. Vincenti, and R. Montereali, “Solid state

detectors based on point defects in lithium fluoride for advanced proton beam diagnostics,” *J. Lumin.* **156**, 170–174 (2014).

¹⁸M. Piccinini, C. Ronsivalle, A. Ampollini, G. Bazzano, L. Picardi, P. Nenzi, E. Trinca, M. Vadrucci, F. Bonfigli, E. Nichelatti, M. A. Vincenti, and R. M. Montereali, “Proton beam spatial distribution and Bragg peak imaging by photoluminescence of color centers in lithium fluoride crystals at the TOP-IMPLART linear accelerator,” *Nucl. Instrum. Methods Phys. Res. A* **872**, 41–51 (2017).

¹⁹B. Marczewska, P. Bilski, T. Nowak, W. Gieszczyk, and M. Kłosowski, “Imaging of proton Bragg peaks in LiF,” *Radiat. Prot. Dosim.* **178**, 333–336 (2018).

²⁰M. Piccinini, E. Nichelatti, C. Ronsivalle, A. Ampollini, G. Bazzano, F. Bonfigli, P. Nenzi, V. Surrenti, E. Trinca, M. Vadrucci, M. A. Vincenti, L. Picardi, and R. M. Montereali, “Visible photoluminescence of color centers in LiF crystals for advanced diagnostics of 18 and 27 MeV proton beams,” *Radiat. Meas.* **124**, 59–62 (2019).

²¹M. Piccinini, E. Nichelatti, A. Ampollini, G. Bazzano, C. De Angelis, S. Della Monaca, P. Nenzi, L. Picardi, C. Ronsivalle, V. Surrenti, E. Trinca, M. Vadrucci, M. A. Vincenti, and R. M. Montereali, “Dose response and Bragg curve reconstruction by radiophotoluminescence of color centers in lithium fluoride crystals irradiated with 35 MeV proton beams from 0.5 to 50 Gy,” *Radiat. Meas.* **133**, 106275 (2020).

²²E. Nichelatti, V. Nigro, M. Piccinini, M. A. Vincenti, A. Ampollini, L. Picardi, C. Ronsivalle, and R. M. Montereali, “Photoluminescent Bragg curves in lithium fluoride thin films on silicon substrates irradiated with a 35 MeV proton beam,” *J. Appl. Phys.* **132**, 014501 (2022).

²³R. M. Montereali, V. Nigro, M. Piccinini, M. A. Vincenti, A. Ampollini, P. Nenzi, C. Ronsivalle, and E. Nichelatti, “Bragg curve detection of low-energy protons by radiophotoluminescence imaging in lithium fluoride thin films,” *Sensors* **23**, 4779 (2023).

²⁴E. Nichelatti, M. Piccinini, A. Ampollini, L. Picardi, C. Ronsivalle, F. Bonfigli, M. A. Vincenti, and R. M. Montereali, “Modelling of photoluminescence from F_2^- and F_3^- colour centres in lithium fluoride irradiated at high doses by low-energy proton beams,” *Opt. Mater.* **89**, 414–418 (2019).

²⁵M. Piccinini, E. Nichelatti, M. A. Vincenti, V. Nigro, C. Ronsivalle, A. Ampollini, P. Nenzi, G. Bazzano, E. Trinca, and R. M. Montereali, “Dynamic range and dose linearity of the radiophotoluminescence intensity in lithium

fluoride crystals irradiated with 2.3 and 26 MeV protons,” *J. Lumin.* **259**, 119833 (2023).

²⁶L. Picardi, A. Ampollini, G. Bazzano, E. Cisbani, F. Ghio, R. M. Montereali, P. Nenzi, M. Piccinini, C. Ronsivalle, F. Santavenere, V. Surrenti, E. Trinca, M. Vadrucci, and E. W. Tafo, “Beam commissioning of the 35 MeV section in an intensity modulated proton linear accelerator for proton therapy,” *Phys. Rev. Accel. Beams* **23**, 020102 (2020).

²⁷The MathWorks Inc., *MATLAB Version 7.10.0 (R2010a)* (The MathWorks Inc., Natick, MA, 2010).

²⁸FLUKA website, see <https://fluka.cern>.

²⁹G. Battistoni, T. Boehlen, F. Cerutti, P. W. Chin, L. S. Esposito, A. Fassò, A. Ferrari, A. Lechner, A. Empl, A. Mairani, A. Mereghetti, P. Garcia Ortega, J. Ranft, S. Roesler, P. R. Sala, V. Vlachoudis, and G. Smirnov, “Overview of the FLUKA code,” *Ann. Nucl. Energy* **82**, 10–18 (2015).

³⁰C. Ahdida, D. Bozzato, D. Calzolari, F. Cerutti, N. Charitonidis, A. Cimmino, A. Coronetti, G. L. D’Alessandro, A. Donadon Servelle, L. S. Esposito, R. Froeschl, R. García Alía, A. Gerbershagen, S. Gilardoni, D. Horváth, G. Hugo, A. Infantino, V. Kouskoura, A. Lechner, B. Lefebvre, G. Lerner, M. Magistris, A. Manousos, G. Moryc, F. Ogallar Ruiz, F. Pozzi, D. Prelicpean, S. Roesler, R. Rossi, M. Sabaté Gilarte, F. Salvat Pujol, P. Schoofs, V. Stránský, C. Theis, A. Tsinganis, R. Versaci, V. Vlachoudis, A. Waets, and M. Witorski, “New capabilities of the FLUKA multi-purpose code,” *Front. Phys.* **9**, 788253 (2022).

³¹V. Vlachoudis, “FLAIR: A powerful but user friendly graphical interface for FLUKA,” in *Proceedings of International Conference on Mathematics, Computational Methods & Reactor Physics (M&C 2009)* (Saratoga Springs, New York, 2009).

³²Wolfram Research Inc., *Mathematica, Version 14.0* (Wolfram Research Inc., Champaign, IL, 2024).

³³OriginLab Corporation. *OriginPro, Version 2021* (OriginLab Corporation, Northampton, MA, 2021).

³⁴K. R. Crandall and M. Weiss, TERA 94/34 ACC 20 internal note (1994).

³⁵T. Bortfeld, “An analytical approximation of the Bragg curve for therapeutic proton beams,” *Med. Phys.* **24**, 2024–2033 (1997).

³⁶J. F. Ziegler, M. D. Ziegler, and J. P. Biersack, “SRIM—The stopping and range of ions in matter (2010),” *Nucl. Instrum. Methods Phys. Res. B* **268**, 1818–1823 (2010).